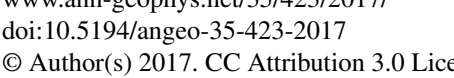
Ann. Geophys., 35, 423–441, 2017 www.ann-geophys.net/35/423/2017/ doi:10.5194/angeo-35-423-2017 © Author(s) 2017. CC Attribution 3.0 License.







# Comparisons between high-resolution profiles of squared refractive index gradient $M^2$ measured by the Middle and Upper Atmosphere Radar and unmanned aerial vehicles (UAVs) during the Shigaraki **UAV-Radar Experiment 2015 campaign**

Hubert Luce<sup>1</sup>, Lakshmi Kantha<sup>3</sup>, Hiroyuki Hashiguchi<sup>2</sup>, Dale Lawrence<sup>3</sup>, Masanori Yabuki<sup>2</sup>, Toshitaka Tsuda<sup>2</sup>, and Tyler Mixa<sup>3</sup>

Correspondence to: Hubert Luce (hubert.luce@univ-tln.fr)

Received: 4 January 2017 - Accepted: 13 February 2017 - Published: 17 March 2017

**Abstract.** New comparisons between the square of the generalized potential refractive index gradient  $M^2$ , estimated from the very high-frequency (VHF) Middle and Upper Atmosphere (MU) Radar, located at Shigaraki, Japan, and unmanned aerial vehicle (UAV) measurements are presented. These comparisons were performed at unprecedented temporal and range resolutions (1–4 min and  $\sim 20$  m, respectively) in the altitude range  $\sim 1.27$ –4.5 km from simultaneous and nearly collocated measurements made during the ShUREX (Shigaraki UAV-Radar Experiment) 2015 campaign. Seven consecutive UAV flights made during daytime on 7 June 2015 were used for this purpose. The MU Radar was operated in range imaging mode for improving the range resolution at vertical incidence (typically a few tens of meters). The proportionality of the radar echo power to  $M^2$  is reported for the first time at such high time and range resolutions for stratified conditions for which Fresnel scatter or a reflection mechanism is expected. In more complex features obtained for a range of turbulent layers generated by shear instabilities or associated with convective cloud cells,  $M^2$  estimated from UAV data does not reproduce observed radar echo power profiles. Proposed interpretations of this discrepancy are presented.

Keywords. Meteorology and atmospheric dynamics (turbulence)

#### 1 Introduction

A very high-frequency (VHF) stratosphere-troposphere radar is mainly sensitive to clear-air refractive index (humidity and temperature) fluctuations on Fourier scales of a length equal to half the radar wavelength (Bragg scale). The backscattering mechanisms depend on the nature of the irregularities to which the radar wave is sensitive. The so-called Bragg backscatter is expected to occur when the radar volume is totally or partially filled by turbulent irregularities (e.g., Tatarski, 1961; Van Zandt et al., 1978). If these irregularities are isotropic on the Bragg scale, the radar returns depend weakly on the beam directions. Under certain conditions, presuming the existence of an inertial subrange, a VHF radar can therefore be employed for retrieving the refractive index structure constant  $C_n^2$  of atmospheric turbulence (e.g., Nästrom and Eaton, 2001).

Fresnel backscatter is another mechanism that occurs preferentially when the beam is oriented vertically due to pronounced horizontal coherency of some irregularities (e.g., Gage and Balsley, 1980; Gage et al., 1985). For this mechanism, the radar volume is assumed to be filled by a random superposition of multiple horizontally stratified and more or less homogeneous layers separated by thin gradient sheets of large horizontal extent (i.e., exceeding the dimensions of the first Fresnel zone). Fresnel backscatter can be dominant near vertical incidence when there is no active turbulence, i.e., when the atmosphere is statically and dynamically

<sup>&</sup>lt;sup>1</sup>Université de Toulon, CNRS/INSU, IRD, Mediterranean Institute of Oceanography (MIO), UM 110, La Garde, France

<sup>&</sup>lt;sup>2</sup>Research Institute for Sustainable Humanosphere, Kyoto University, Kyoto, Japan

<sup>&</sup>lt;sup>3</sup>Department of Aerospace Engineering Sciences, University of Colorado Boulder, Boulder, Colorado, USA

stable, as is often the case in the lower stratosphere (e.g., Röttger and Larsen, 1990). The Fresnel reflection mechanism is an asymptotic form of the Fresnel scatter since it assumes the presence of a few isolated or dominant gradient sheets in the radar volume that would cause partial reflection of the incident radar wave (Röttger and Liu, 1978). While Fresnel scatter would be quite pertinent for coarse radar range resolutions (say  $> \sim 150 \,\mathrm{m}$  as is typically the case for VHF radars), Fresnel reflection may be relevant if high-performance radar systems are used. For example, the Jicamarca SOUSY 53.5 MHz radar can now be operated at a vertical resolution of 37.5 m (Woodman et al., 2007) by an effective reduction in the transmitted pulse duration and increase in the receiver bandwidth. With such a good range resolution, the alternation of sharp temperature gradient sheets and weakly stratified layers, as revealed by high-resolution temperature sensors (e.g., Dalaudier et al., 1994) or even by the currently used 1 Hz radiosondes, can potentially be detected. When transmitting longer pulses, radar imaging techniques using frequency diversity can constitute alternative means for improving the range resolution. Similar resolution performance can be reached and isolated gradients can be detected (e.g., Luce et al., 2010, 2017).

The real atmosphere likely involves more complex mechanisms than Bragg scatter and Fresnel scatter or reflection. Many complications due to the coexistence of coherent and turbulent irregularities on the same scales in the radar volume, varying degrees of horizontal coherence, the modulation of the field by various internal waves and instabilities, and so on, can make the identification of the different types of mechanisms difficult, when the radar echoes are not isotropic. However, soon after the development of ST radars, concurrent measurements of atmospheric parameters from balloons launched near radar sites have been made for interpreting the radar echoes, with some notable successes (e.g., Röttger and Larsen, 1990; Gage, 1990). In particular, a large number of studies have reported a close relationship between the echo power  $P_{v}$  at vertical incidence (hereafter,  $P_{\rm v}$  will refer to the echo power corrected from the range attenuation effects by the product, i.e.,  $P \times z^2$ , where P is the echo power and z is the altitude) and the square of the vertical gradient of the generalized potential refractive index  $M^2$ (Ottersten, 1969) in clear-air conditions, calculated from balloon data at the vertical resolution of the radar measurements (e.g., Röttger, 1979; Larsen and Röttger, 1983, 1985; Tsuda et al., 1988; Hocking and Mu, 1997; Hooper and Thomas, 1998; Low et al., 1998; Hooper et al., 2004; Vaughan et al., 1995; Luce et al., 2007; Kirkwood et al., 2010). But radiosonde measurements provide "instantaneous" values only along the path of the balloon, which tends to move as much as a few tens of kilometers or more away from the radar due to wind drift. In order to overcome this drawback, the radar signals are very often averaged over periods corresponding to the balloon flight duration in the altitude range of interest (i.e., typically  $\sim 30$ –60 min) for comparison with balloon measurements. The results of the comparison are thus usually analyzed and interpreted only in a statistical sense.

Possible discrepancies at some individual altitudes between  $P_v$  and  $M^2$  are generally not interpreted (which is consistent with the nature of a statistical comparison), for a number of possible reasons: (1) there are instrumental artifacts, themselves of multiple origins, (2) radars and balloons do not probe the atmosphere at the same place and same time, (3) the model is not relevant for these altitudes. The importance of hypothesis (2) is extremely difficult to evaluate, making hypothesis (3) impossible to ascertain since it all depends on the horizontal extent of the gradients that may be vertical-scale dependent. In addition, tilts of the isentropic surfaces due to baroclinic conditions or internal wave motions can produce apparent discrepancies that would not appear if altitude coordinates were replaced by the potential temperature  $\theta$  coordinates (e.g., Koishi and Shiotani, 2012). However, hypothesis (3) could be suggested for the important case of saturated conditions (Vaughan and Worthington, 2000). A discrepancy is indeed expected because  $M^2$  is derived from the conservation of  $\theta$ , which is not true for saturated conditions.

The statistically close relationship between  $P_v$  and  $M^2$  reported in the literature does not provide any information on the backscatter mechanisms if they are considered separately. Indeed, all the aforementioned backscattering models predict that  $P_v$  is proportional to  $M^2$ , but  $P_v$  is also proportional to specific parameters depending on the model (see Appendix A):

$$L_{\rm O}^{4/3}$$
 for the turbulent scatter, (1a)

$$F(\lambda)^2$$
 for the Fresnel scatter, (1b)

$$G(\lambda, \Delta L)^2$$
 for the Fresnel reflection, (1c)

where  $L_{\rm O}$  is an outer scale of turbulence defined as the largest scale for which the turbulence is isotropic (Silverman, 1956; Tatarski, 1961),  $F(\lambda)$  is a wavelength-dependent factor of proportionality, which relates the magnitude of the  $\lambda/2$  harmonic component of M over the altitude interval  $\Delta z$  (e.g., Gage et al., 1985), and  $G(\lambda, \Delta L)$  is a wavelength-dependent factor, which is a function of the depth *and the shape* of the refractive index gradient embedded within the radar volume.

It follows therefore that, for a given model and a fixed  $M^2$ ,  $P_{\rm v}$  can theoretically strongly vary over many decades (especially for the Fresnel reflection model, which is strongly gradient shape-dependent (e.g., Woodman and Chu, 1989; Luce et al., 1995). In addition, Fresnel and turbulent scatter can alternately dominate in altitude depending on the local stability conditions, making it difficult, in principle, to reveal the proportionality between  $P_{\rm v}$  and  $M^2$ . Despite these theoretical difficulties, all the aforementioned studies concluded that  $P_{\rm v} \sim M^2$  without considering the nature of the backscattering mechanism. No attempt was generally made to distinguish between the different mechanisms.

In the present work, the relationship between  $P_v$  and  $M^2$ is revisited at unprecedented time and range resolutions, by using original datasets collected from the Middle and Upper Atmosphere (MU) Radar operating in range imaging mode and from small unmanned aerial vehicles (UAVs) flown in the vicinity of the radar (Kantha et al., 2017). Atmospheric measurements by small, low-cost UAVs have become increasingly popular in recent years (e.g., van den Kroonenberg et al., 2008; Lawrence et al., 2008; Balsley et al., 2013; Bonin et al., 2015; Scipion et al., 2016) because they offer many potentials and advantages for atmospheric studies (e.g., Lawrence and Balsley, 2013). During a field campaign called ShUREX (Shigaraki UAV-Radar Experiment) carried out in June 2015 at the MU Shigaraki Observatory (Kyoto University, Japan), instrumented UAVs measured pressure, temperature and relative humidity (PTU) and turbulence parameters in the lower atmosphere (up to about 4-5 km) at a horizontal distance of about 1.0 km from the MU Radar (Kantha et al., 2017). The data collected during this campaign provides the basis for this paper.

The present work also aims to confirm the relevance of the range imaging technique for range resolution improvement and the effectiveness of the UAV technique for probing the vertical structure of the temperature and humidity fields. Comparisons between  $P_v$  and  $M^2$  are made at a vertical sampling of 20 m and a time averaging of a few minutes (1–4 min) of the radar measurements along the vertical path of the UAVs from 1.275 km up to  $\sim 4.5$  km a.s.l. Comparisons at such resolutions should minimize the effects of horizontal inhomogeneity of the temperature and humidity fields when interpreting the difference between the two datasets. We use the datasets collected on 7 June 2015 from 05:30 to 19:00 LT, during which seven consecutive UAV flights were successfully made. The UAV trajectory was mainly a helical ascent and descent of 100-150 m diameter, near or above the launching site so that comparisons could be made for both ascent and descent up to  $\sim 4-5$  km in altitude, with little difference in time. Three Vaisala radiosondes were also launched simultaneously during some UAV flights. In addition, a micro-pulse lidar (MPL) was continuously operated for cloud detection. The MPL is an autonomous laser radar system originally developed at the National Aeronautics and Space Administration (NASA) Goddard Space Flight Center (GSFC) (Spinhirne, 1993). We used the MPL-4 system (Sigma Space Corporation, USA) that had a measurement wavelength of 527 nm. Data averaged over each 20 s were acquired with a 15 m range resolution. Vertical resolution of the lidar observation was approximately 13 m since the telescope was steered 30° off zenith. This study makes use of the normalized relative backscatter estimated from the raw signals as described in Campbell et al. (2002). The results of a more detailed analysis of each flight will be described in a separate paper.

The instruments and data processing for retrieving  $M^2$  profiles from radar UAV data are described in Sect. 2. Com-

Table 1. MU Radar parameters used during the ShUREX campaign.

Parameter	
Beam directions	(0°, 0°), (0°, 0°), (0°, 0°), (0°, 0°), (0°, 0°), (0°, 10°), (45°, 10°), (90°, 10°), (135°, 10°), (180°, 10°)
Radar frequencies (MHz)	46.00, 46.25, 46.50, 46.75, 47.00
Inter-pulse period (µs)	400
Sub-pulse duration (µs)	1
Pulse coding	16 bit optimal code
Range resolution (m)	150
Height sampling (m)	5
Number of gates	128
Coherent integration number	32
Incoherent integration number	(time series)
Number of fast	
Fourier transform points	128
Acquisition time (s)	16.384*
Time sampling (s)	4.096
Nyquist frequency (Hz)	3.9063
Velocity aliasing (ms <sup>-1</sup> )	12.6

<sup>\*</sup> Acquisition of a time series of 128 points for each direction, but the effective time resolution is about half ( $\sim$  8 s) due to Hanning windowing of the time series.

parison results are shown in Sect. 3, and their discussion is in Sect. 4.

#### 2 Instruments and data processing

### 2.1 The MU Radar

The MU Radar is a 46.5 MHz beam-steering Doppler pulsed radar located at the Shigaraki MU Observatory (34.85° N, 136.10° E), Japan (Fukao et al., 1990). The radar parameters used during the campaign are listed in Table 1. The radar was operating in range imaging mode when pointing vertically. This observational mode consists in transmitting several closely spaced frequencies pulse to pulse. During ShUREX 2015, five equally spaced frequencies were selected between 46.0 and 47.0 MHz with a sub-pulse width of 1 µs and a 16 bit optimal code. The radar parameter configuration used provides an effective range resolution of a few tens of meters with the Capon processing method for a high signal-to-noise ratio (SNR; e.g., Luce et al., 2001). As an aside to the main objectives of ShUREX, the UAV signature in the radar echo power images could be used for confirming this performance (Luce et al., 2017).

The radar parameters were set up so that one high-resolution profile of the echo power at vertical incidence was acquired from the altitude of 1.27 up to  $20.465 \, \mathrm{km}$  (a.s.l.) every  $\sim 4 \, \mathrm{s}$  at an effective time resolution of  $\sim 8 \, \mathrm{s}$  (see Table 1). The radar measurements in range imaging mode were inter-

Table 2. Brief description of the UAV flights (7 June 2015).

UAV flight	Launch time (LT)	Maximum height
4	05:44:00	3.9
5	07:14:11	4.3
6	09:44:58	3.5
7	10:55:36	4.0
8	12:55:28	3.3
9	15:34:41	3.3
10	17:33:43	4.4

rupted every  $\sim 35\,\mathrm{min}$  for a few minutes. In addition, five oblique beams steered at  $10^\circ$  off zenith were included for estimating additional parameters such as horizontal winds and wind shear and echo power aspect sensitivity at a range resolution of  $150\,\mathrm{m}$ .

#### 2.2 DataHawk UAV

The DataHawk UAVs are small (less than 1 m wingspan and about 700 g mass), inexpensive (USD  $\sim$  1000 to 2000) airplanes equipped with autopilots capable of executing preplanned trajectories for measuring atmospheric parameters. They use GPS for navigation. The design of the DataHawk UAV, the characteristics of ground support components and some data collected from these systems were described by Lawrence and Balsley (2013) and Balsley et al. (2013).

During the campaign, the launching site was some fallow land located at about 1.0 km southeast from MU Radar (Fig. 1). The UAV flights described in the present work were flying in a helical pattern of 100–150 m diameter during ascent up to  $\sim 4.0$  km and during descent for 60–90 min depending on the climb rate (typically  $\sim 2\,\mathrm{m\,s^{-1}}$ ). The Data-Hawk UAVs were equipped with multiple sensors (Kantha et al., 2017), among which there were IMET sensors capable of measuring pressure, temperature and relative humidity at 1 Hz. The time response of the temperature sensor is  $\sim 2\,\mathrm{s}$  at 1000 hPa, its resolution is less than 0.01 K and accuracy is about 0.2 K. The time response of the humidity sensor is  $\sim 2\,\mathrm{s}$  at 25 °C and 60 s at -35 °C; its resolution is less than 0.1 % and accuracy is about 5 %.

A total of 19 flights was made during the ShUREX 2015 campaign from 5 to 13 June. The main characteristics of the six UAV flights made on 7 June and analyzed in the present study are displayed in Table 2.

# 2.3 Estimating $M^2$ from radar and UAV data

### **2.3.1** Theory

The vertical gradient M of the generalized potential refractive index used in radar signal analysis is defined for non-

saturated air as

$$M = -77.6 \times 10^{-6} \left(\frac{p}{T}\right) \left\{ \frac{N^2}{g} + \frac{15500q}{T} \left[ \frac{N^2}{g} - \left(\frac{1}{2q}\right) \frac{dq}{dz} \right] \right\},\tag{2}$$

where  $N^2 = \frac{g}{T} \left( \frac{dT}{dz} + \Gamma \right)$  is the square of the buoyancy frequency,  $\Gamma$ , the dry adiabatic lapse rate (K m<sup>-1</sup>), T, the temperature (K), p, the pressure (hPa), q, the specific humidity (g g<sup>-1</sup>), and g, the gravitational acceleration.

The various models of backscattering mechanisms suggest the following relationship between  $M^2$  and radar echo power  $P_v$ :

$$M^2 = KP \cdot z^2 = K\dot{P}_v,\tag{3}$$

where z is altitude and K is a coefficient that depends on some radar parameters but should also depend strongly on the backscatter model used and on some salient properties of the scatterers (see Appendix A). In contrast, all the aforementioned studies performed at a vertical resolution > 150 m concluded that the factor K could be considered a constant, which depends only on radar parameters, at least to a first approximation and from a statistical point of view. Luce et al. (2007) performed six comparisons for stratospheric heights (dry atmosphere) with the MU Radar in range imaging mode at a vertical sampling of 50 m and found a constant factor ( $K = -231 \, dB$ ) that fitted the six case studies made at different times of the day. The radar parameters involved in Eq. (3) used for the experiment described by Luce et al. (2007) were the same as those used during ShUREX 2015. It was thus decided to apply the same value of K to all the comparison results presented here, even if the profiles were not compared with the same time averaging and range sampling and were not gathered in the same altitude range (which here is the lower troposphere, where humidity contribution could dominate). The relevance of this empirical calibration will be discussed in the results section.

#### 2.3.2 Practical estimation methods from UAV data

Pseudo-vertical profiles of PTU sampled at a rate of 1 Hz were used to estimate the variables necessary for applying Eq. (2). The ascent and descent rate of the UAVs was typically 2 m s<sup>-1</sup> so that all the PTU profiles were first resampled at constant steps of 2 m. The resampled profiles were then filtered by using a low-pass filter with a cutoff wavelength of 40 m, so that a vertical resolution of 20 m could be achieved for PTU data. The vertical derivatives in Eq. (2) were obtained by using a three-point central scheme.  $M^2$  profiles were estimated during ascent and descent for each of the seven UAV flights.

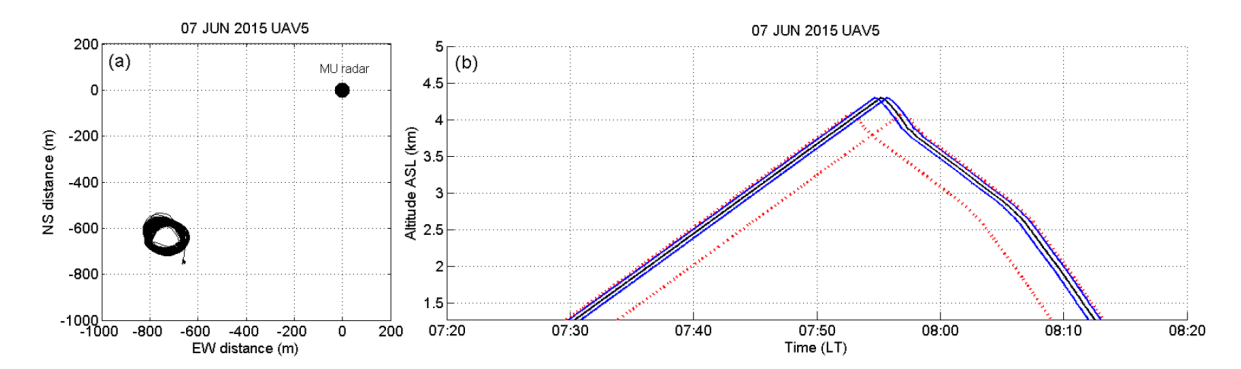


**Figure 1.** (a) Plot of GPS positions of UAV5 with respect to MU Radar antenna location. During ascent and descent, the UAVs were flying in a helical pattern of 100–150 m diameter. The black dot indicates the position of the MU Radar antenna array. (b) Altitude above sea level (black; a.s.l.) vs. time plot of flight UAV5 launched at 07:14:11 LT on 7 June 2015. The blue solid and red dotted lines show the two time intervals used for averaging the radar data at each altitude.

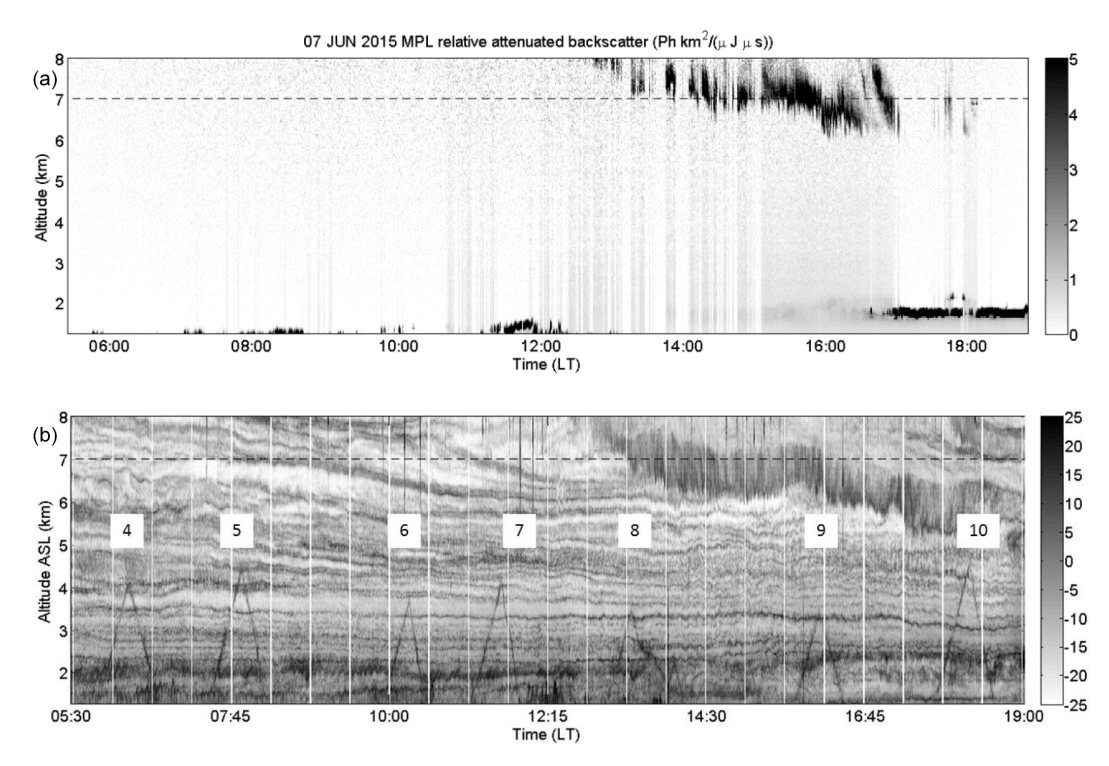


**Figure 2.** (a) Time-height plot of MPL normalized relative backscatter (counts km<sup>2</sup>  $\mu$ J<sup>-1</sup>  $\mu$ s<sup>-1</sup>) from 05:30 to 19:00 LT on 7 June 2015. (b) The corresponding image of MU Radar echo power  $P_{\rm V}$  (dB, arbitrary level) at vertical incidence. The labels 4 to 10 indicate the UAV flights, whose tracks are clearly visible as triangles in the lower part of the image.

#### 2.3.3 Practical estimation methods from radar data

Our strategy is to compare pseudo-vertical profiles of  $M_{\rm UAV}^2$  with reconstructed profiles estimated from radar echo power, measured at a horizontal distance between UAV position and radar volume that is as small as possible and at the same time. The helical trajectory of the UAV from the ground up to  $\sim 5.0\,\rm km$  at a horizontal distance of  $\sim 1.0\,\rm km$  is such that the spurious echoes from UAV did not affect the radar measurements at the flight altitude and time of the UAV. For ex-

ample, Fig. 1 describes the characteristics of flight UAV5. The other UAVs (4, 6–10) had a similar flight mode, except for UAV4 and UAV8, during which a first descent was followed by a short ascent and a second descent (see Fig. 2, labels 4 and 8; it is imperceptible for UAV4). Panel a shows a plot of the GPS positions of the UAV with respect to the MU Radar antenna location. Panel b shows the altitude above sea level of the UAV as a function of time (black line). The blue solid and red dotted lines represent the time intervals used for calculating the temporal average of  $M_{\rm radar}^2$  at the altitude

of the UAV. Time averages were arbitrarily set to 1 and 4 min (corresponding to  $\sim$  14 and  $\sim$  59 samples, respectively), i.e.,  $\pm 30\,\mathrm{s}$  and  $\pm 2\,\mathrm{min}$  around the time of the UAV flight. The 1 min averaged profile is treated as a nearly instantaneous profile. The 4 min averaged profile should be subject to sporadic features and horizontal inhomogeneity a little bit less but a small time shift ( $\sim$  1.5 min) has to be introduced in order to avoid UAV contaminations in the radar echoes (occurring along the green line of Fig. 1). Therefore, the mean values are not exactly centered at the time of the UAV. Finally, the standard deviation of the samples was estimated from the 4 min datasets for illustrating the time variability of  $M_{\mathrm{radar}}^2$  for each sampled altitude. For high SNR values (as is the case here, typically 20–50 dB; not shown), this variability is expected to exceed the variability due to estimation errors.

#### 3 Observation results

#### 3.1 General context

Prior to presenting  $M^2$  comparison results, we first describe (Fig. 2b) the main characteristics of the radar echo power at vertical incidence in the altitude range 1.27 to 8.00 km on 7 June 2015, from 05:30 to 19:00 LT, during which the seven UAV flights were made. The corresponding MPL data are shown in Fig. 2a. The labels in white rectangles indicate the UAV flights (Table 2). The triangle-shaped signature of the UAV echoes can be clearly seen in the radar echo power image. Luce et al. (2017) studied their properties for demonstrating the performance of the range imaging technique in detail.

The main features of the atmospheric echoes can be briefly summarized as follows.

- 1. Below 2.5 km: intense echoes with more or less irregular patterns. A persistent layer can be noted around 2.0 km throughout the observation period and a second one around 1.5 km until 12:00 LT at least. The MPL observations indicate clouds up to  $\sim$  1.5 km in the convective boundary layer.
- 2. Between 2.5 and 4.5 km: a layered structure revealing a persistent stratification with multiple sheets of gradients of temperature and humidity.
- 3. Above 4.5 km: a complex evolution suggesting the approach of a meteorological front (e.g., Lawson et al., 2011). Multiple bands of descending radar echo layers from ~08:00 LT below 8.0 km are followed by a descending cloud layer seen by the MPL from 12:30 LT below 8.0 km (top of Fig. 2). A proxy of the cloud base around 14:30 LT is given by the dashed line (7.0 km) for easy reference. A radar echo layer of 1.0–1.5 km in depth can be noted at the cloud base and is a signature of a mid-level cloud-base turbulence (MCT) layer developing due to a convective instability below a cloudy

frontal zone (e.g., Luce et al., 2010; Kudo, 2013; Kudo et al., 2015). The probable convective motions inside the layer are likely the cause of small-scale internal wave oscillations seen below the turbulent layer down to 2.0 km at least since they coincide with its passage (oscillations start from  $\sim$  14:15 LT). UAV9 and UAV10 could not probe the deep turbulent layer but were probing the thin oscillating layers. The conditions met by these UAVs thus contrast with those met during flights UAV4 to 8, for which the vertical displacements were smaller.

#### 3.2 UAV4 and UAV6

Two close-ups of a radar echo power map (Fig. 2) are shown in Fig. 3 for two representative UAV flights (UAV4, panel a, UAV6, panel b) for easier interpretation of the radar images. Figure 4 shows

- the corresponding profiles of temperature and relative humidity measured during ascent (blue line) and descent (red line).
- 2. vertical profiles of horizontal wind shear *S* calculated at a vertical resolution of 150 m from 30 min averaged zonal and meridional wind components estimated from MU Radar Doppler data, using the six beam directions.
- 3. vertical profiles of Richardson number  $Ri = N^2/S^2$ , where  $N^2$  is the square of the Brünt–Vaïsälä frequency and  $S^2$  is the square of the mean shear. Two (dry)  $N^2$  profiles were first estimated from the temperature profiles measured during ascent and descent at a vertical resolution of 150 m and then averaged for estimating a single profile of Ri.
- 4. 30 min averaged profiles of the radar aspect sensitivity defined as  $AR = P_{\text{vert}}$  (dB)  $-P_{\text{obl}}$  (dB), where  $P_{\text{vert}}$  is the vertical echo power at the resolution of 150 m and  $P_{\text{obl}}$  is the mean oblique echo power defined as the average of powers measured from the five oblique beams (see Table 1).
- 5. 30 min averaged profiles of variance  $\sigma_{turb}^2$  of Doppler spectra measured with the vertical beam at a vertical resolution of 150 m. The nonturbulent contribution due to beam-broadening effects has been removed by using a standard procedure (Wilson et al., 2014).

The time averages were performed from 06:07 and 10:02 LT for UAV4 and UAV6, respectively. Contrary to the strategy used for  $M^2$  studies, time averaging was applied here in order to reduce possible biases on wind estimates (due to the inhomogeneity of the wind field on short timescales). The calculated profiles shown in Fig. 4 are only indicative since the resolutions are quite poor and are intended only for interpreting or confirming the interpretation of the radar images of echo power shown in Fig. 3.

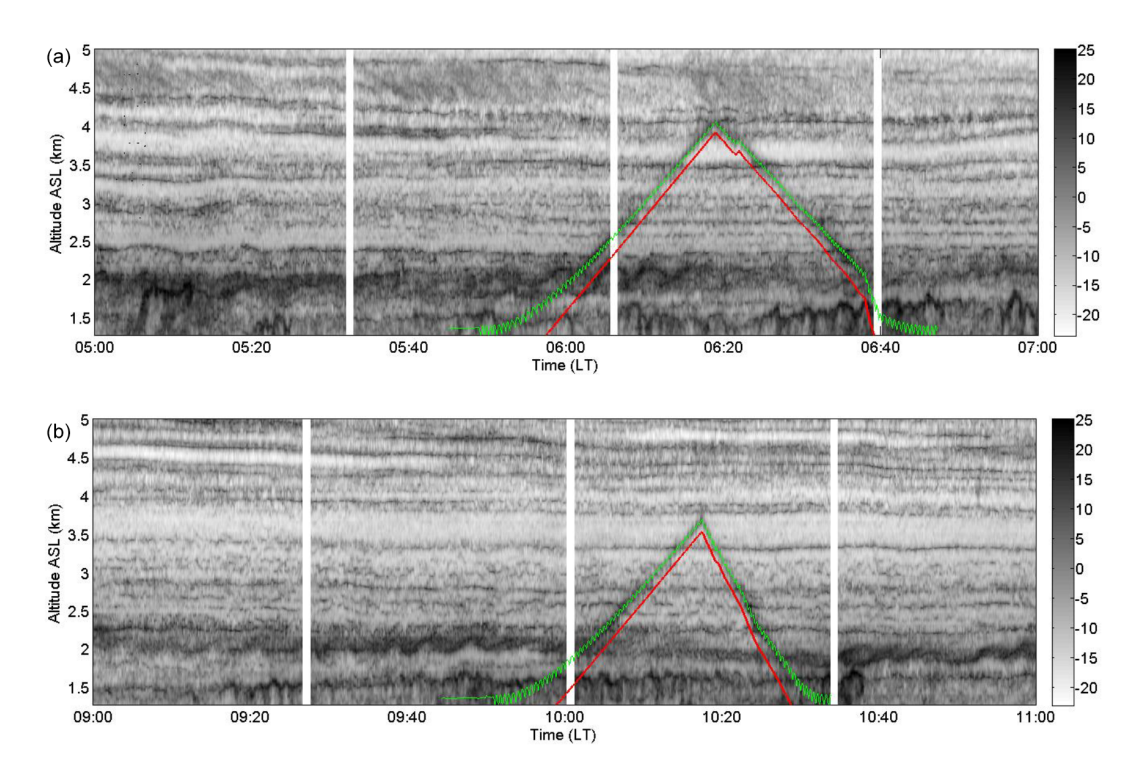


**Figure 3.** (a) Time-height plot of MU Radar echo power at vertical incidence from 05:00 to 07:00 LT on 7 June 2015, corresponding to flight UAV4. The red (green) line shows the altitude (distance) of the UAV versus time. (b) Same information but for flight UAV6.

From Figs. 3 and 4, it appears that the lower atmosphere in the range 1.27 to 5.00 km could be schematically divided into three distinct regions labeled CL, KH and ST.

- 1. The "CL region" refers to echoing structures reminiscent of cloudy convective cells very similar to those classically reported by frequency-modulatedcontinuous-wave (FM-CW) radar observations (e.g., Gossard, 1990). These cells were present during the first half of the observation period. They were likely associated with a convective and moist (cloudy) boundary layer up to  $\sim 1.5$  to 1.7 km as indicated by the humidity profile in Fig. 4 and suggested by the MPL data (Fig. 2). The top of the CL region is only indicative for UAV4 in Fig. 4 since it differs strongly between ascent and descent. Updrafts and downdrafts of  $\sim 0.5 \,\mathrm{m\,s^{-1}}$  were observed by the MU Radar in the convective cell environment (not shown). The largest echoes are detected at the edges of the cells where the humidity gradient was intense. A fish-eye camera at the radar site pointing vertically up revealed cumulus-type clouds during this period (not shown). The CL region is associated with low aspect sensitivity and enhanced  $\sigma_{\text{turb}}^2$  that may indicate enhanced turbulence.
- 2. The "KH region" ( $\sim$  1.7 to 2.5 km) refers to an altitude range where Kelvin–Helmholtz shear instabilities occurred. KH braids of various depths associated with

enhanced echoes can be clearly seen around the ascent of UAV4, and they were capped by more or less clearly defined thin layers of enhanced echoes up to a height of 2.5 km. Similar structures and cat's eye patterns can be seen just before and after flight UAV6. The horizontal wavelength of the KH billows can be deduced from wind speed measured by MU Radar at the altitude of the critical level, where the phase speed of the KH wave is equal to background wind speed. It was found that the wind shear and wind vectors were in the same direction so that the horizontal wavelength can be calculated as simply the product of the wind speed and the time spacing between the billows in the radar image. The horizontal wavelength was found to be  $\sim 870\,\mathrm{m}$ . The KH region was separated from the CL region by a narrow range of weak echoes at the bottom. At the height of  $\sim 2.5$  km, a very thin and persistent echo layer due to a sharp temperature and humidity gradient (Fig. 4) was present defining the bottom of the ST region defined be-

Despite the coarse resolution of the observations, all the parameters shown in Fig. 4 are consistent with the hypothesis of shear-generated turbulence: enhancement of the horizontal wind shear, minimum Ri (somewhat larger than 0.25, but Ri is a scale-dependent parameter; see Balsley et al., 2008), isotropic echoes (aspect sensitivity close to 0 dB) and enhancement of  $\sigma_{\rm turb}^2$ .

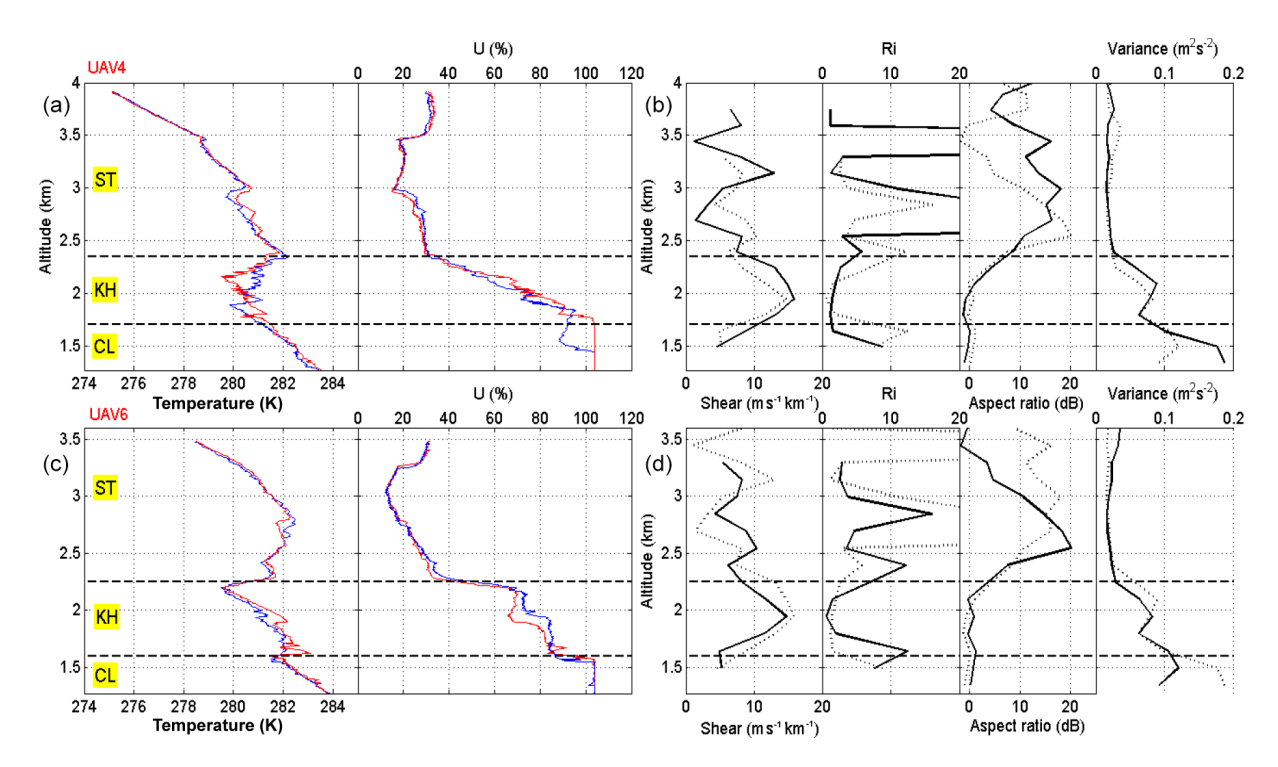


**Figure 4.** (a, b) From left to right: temperature and humidity profiles during ascent (blue) and descent (red) of UAV4, vertical profiles of horizontal wind shear, Richardson number, radar aspect sensitivity and the turbulent contribution to the variance of Doppler spectra. (c, d) Same information but for flight UAV6. The labels CL, KH and ST and horizontal dashed lines refer to altitude ranges discussed in the text. For easy comparisons between the two flights, the dotted profiles for UAV4 (UAV6) show the profiles obtained from UAV6 (UAV4).

KH billows appeared many times during the observation period (see Fig. 2), but sporadically, indicating that the billows were organized into patches and were not uniformly distributed over a large horizontal domain. During the descent of UAV6, there was no evidence of KH billows of similar scales, despite dynamic conditions similar to those met during UAV4. Rather, the radar echo power image shows a double-layer structure with a minimum echo power at the center ( $\sim 2.0 \,\mathrm{km}$ ). The temperature and humidity profiles during flights UAV4 and UAV6 show distinct features around 2.0 km. During the ascent and descent of UAV6, the temperature gradient was nearly adiabatic, and the relative humidity profiles show step-like structures with nearly constant values in between. Therefore, a late stage of turbulent mixing (homogenization) may have been observed during UAV6.

3. The "ST region" ( $\sim$  2.5 to 4.0 km) refers to an altitude range where thin stratified persistent echo layers were observed. This region coincides with a drier atmosphere and with thin layers of sharp temperature and humidity gradients. Relatively blurred KH braid patterns of weak intensity between two persistent and thin echo layers can also be distinguished above  $\sim$  4.5 km around flight UAV4 (top of Fig. 3).

## 3.3 Results of $M^2$ comparisons

Figure 5a–g show  $M_{\rm UAV}^2$  profiles (blue curves) superimposed on  $M_{\text{radar}}^2$  profiles (black curves) for each of the seven UAV flights on 7 June 2015. The left and right panels show the results for ascent and descent, respectively. The 1 min (4 min) averaged  $M_{\rm radar}^2$  profiles are shown in solid (dotted) lines and the standard deviation (time variability over 4 min) in horizontal gray bars for each altitude. The three regions labeled CL, KH and ST are indicated when present. Horizontal dashed red lines show the cloud top related to the convective boundary layer (CBL) given by UAV relative humidity sensor measurements, and the altitude of the interface between the KH and ST regions is defined by the mean position of the steep negative humidity gradient at the top of the KH layer. Note that the vertical extent of the KH region differs slightly from the vertical separation between the two interfaces. In addition, the corresponding time-height plot of echo power during each UAV flight is shown in a small inset for easy reference. A higher-level cloud layer detected by MPL from  $\sim 14:00\,\mathrm{LT}$  modified the three-region structure during UAV9 and UAV10. The corresponding MPL observations are shown for these two flights.

The analysis of the results shown in Fig. 5a–g indicates the following points.

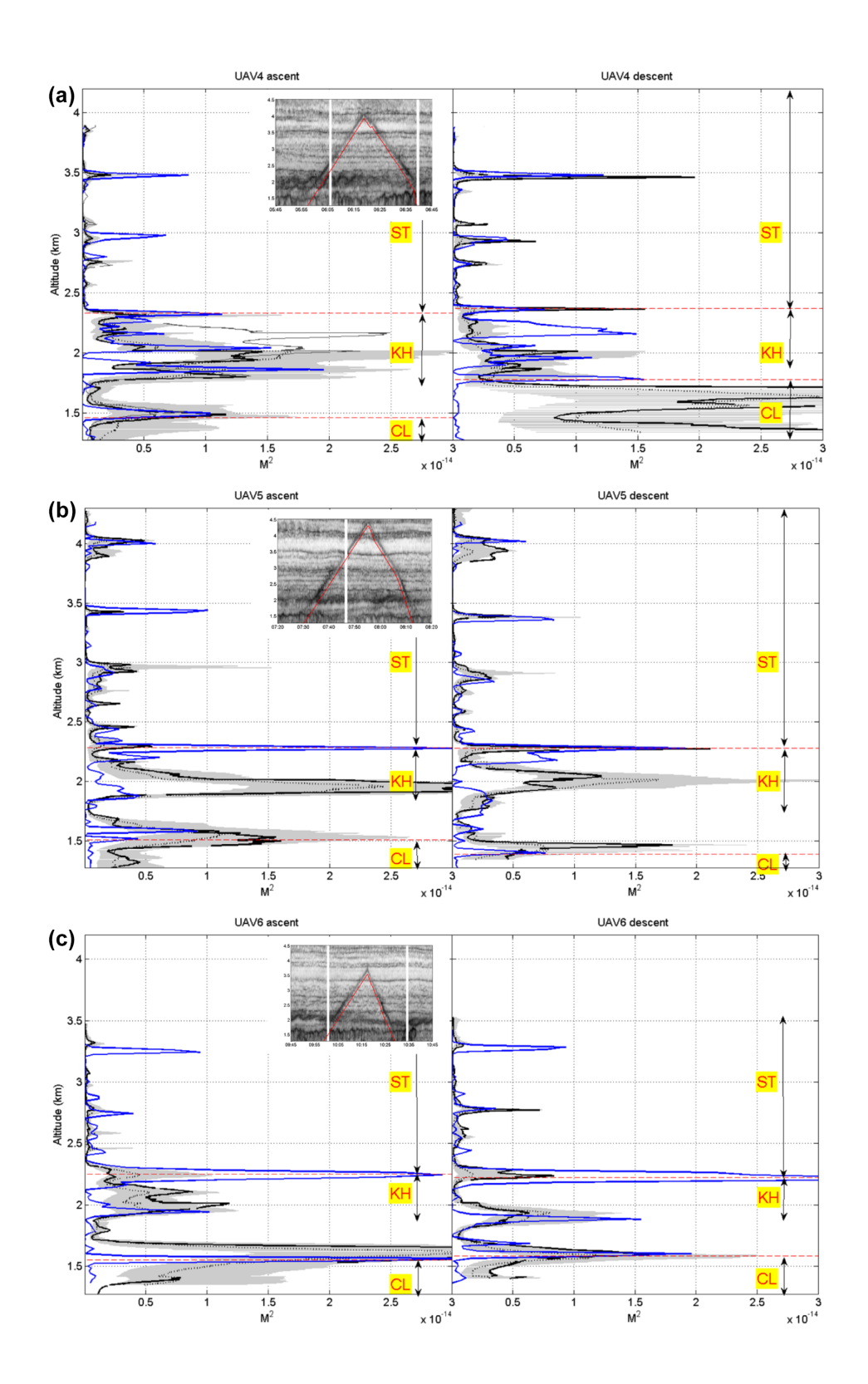


Figure 5.

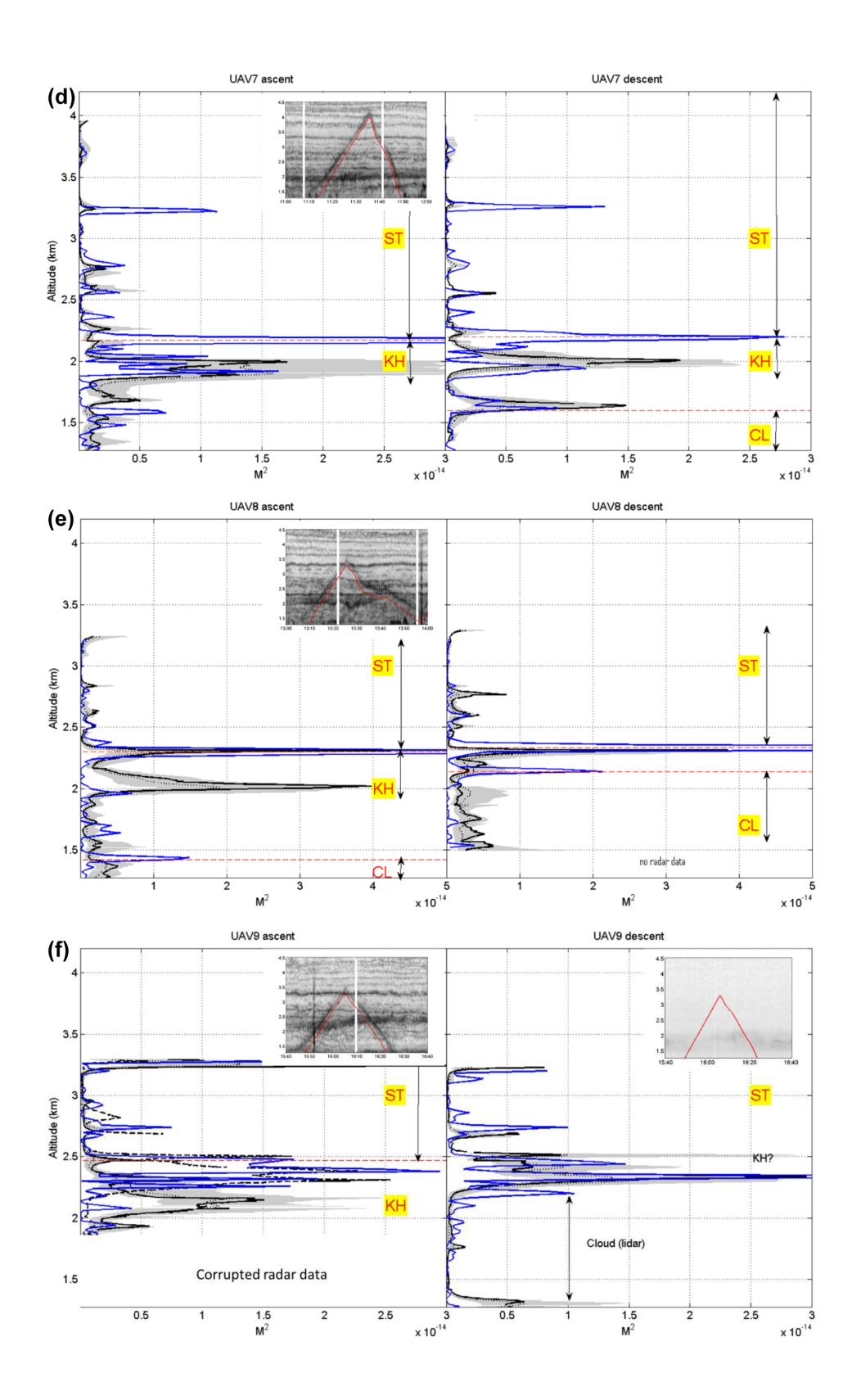
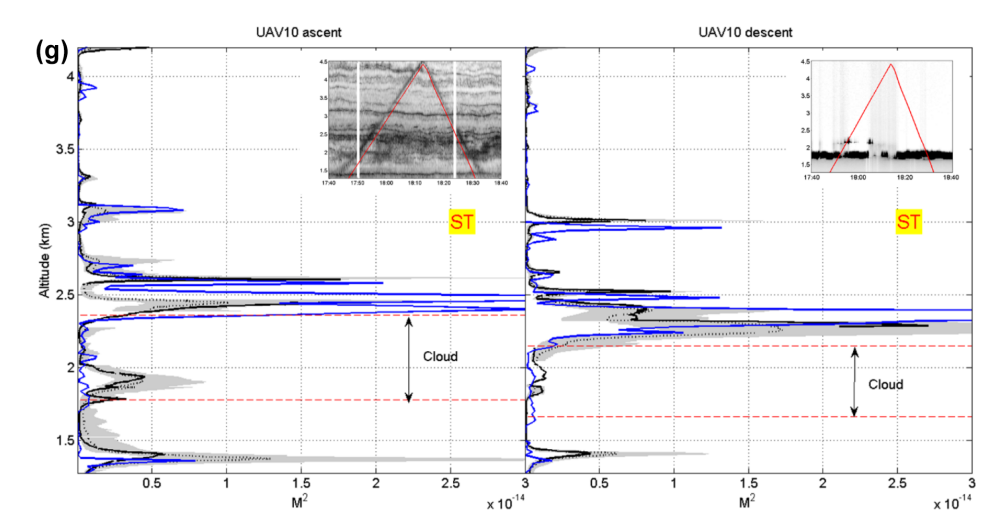
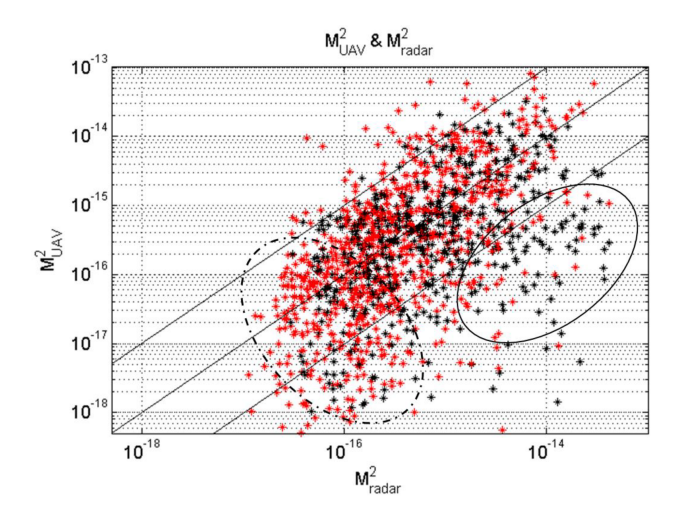


Figure 5.



**Figure 5.** (a)  $M_{\rm UAV}^2$  (blue) and  $M_{\rm radar}^2$  (solid black: 1 min averaged; dotted black: 4 min averaged) profiles for flight UAV4. The thin black line is from radar data during the flight, and the bold black line is from radar data collected 7 min before. Gray color shows the standard deviation over 4 min. The lower red dashed line shows the top of the CL region and the higher one the interface between the KH and ST regions. (b) Same as (a) (without the thin black line) but for UAV5. (c) Same as (b) but for UAV6. (d) Same as (b) but for UAV7. (e) Same as (b) but for UAV8. (f) Same as (b) but for UAV9. (g) Same as (b) but for UAV10.



**Figure 6.**  $M_{\rm radar}^2$  plotted against  $M_{\rm UAV}^2$  for the seven UAV flights on 7 June 2015. Red markers correspond to data in the ST region. The (solid) ellipse focuses on the values mainly obtained in the KH and CL regions. The (dashed) ellipse shows the low values biased by the limitations of power minima.

- 1. An overall good agreement between the characteristics of the peaks of  $M_{\text{UAV}}^2$  and  $M_{\text{radar}}^2$  in the ST region.
  - a. The amplitude of the fluctuations (on linear scales) correspond well, and the levels of  $M_{\rm radar}^2$  peaks generally coincide within a factor of 1 to 6 (very often less than 2) in magnitude. Therefore, the empirical calibration of  $M_{\rm radar}^2$  based on earlier comparisons made at stratospheric heights (Luce et al., 2007) is quite appropriate. The present study therefore is the

- first successful attempt to retrieve absolute values of  $M^2$  from radar data at such high time and range resolutions. These results also confirm that at such unprecedented high resolutions, the vertical echo power is strongly dominated by  $M^2$ , when Fresnel scatter or reflection occurs as is expected to be the case in the ST region. However, it still contradicts the prediction of the models (see Appendix A). The present results do not provide clarification of this issue.
- b. Most peaks are separated by deeper regions of low-level  $M^2$  so that the correspondence cannot be fortuitous, even when there are slight altitude differences at times (either due to technical issues, e.g., GPS altitude errors, or due to atmospheric origin such as slight tilts or vertical displacements of the refractive index gradients). These altitude differences mostly occur during UAV9 and UAV10. They were expected due to the more pronounced and high-frequency vertical oscillations produced by small-scale waves during these flights (see Fig. 2). In general, the agreement in position reveals the excellent calibration of the MU Radar in altitude after the slight correction made by Luce et al. (2017) from the same dataset.
- c. Incidentally, these results still confirm that the range imaging technique does not produce visible "ghost" peaks due to some kind of aliasing effects that could make the technique subject to hypotheses on the atmospheric scatterers. Some rare  $M_{\rm radar}^2$  peaks do not match the  $M_{\rm LIAV}^2$  peaks in the ST re-

gion (Fig. 5a, UAV4 descent,  $\sim 3.1 \,\mathrm{km}$ ), but the opposite is also true (e.g., Fig. 5c, UAV6 ascent). Therefore, the present study constitutes an additional validation of the range imaging technique.

We found low correlation coefficients between  $M_{\rm UAV}^2$  and  $M_{\rm radar}^2$  profiles for all regions (not shown) despite the close resemblance between these profiles. However, these low correlations in the ST region are likely mainly due to small altitude offsets between the thin peaks. Figure 6 shows a scatterplot of  $M_{\rm radar}^2$  vs.  $M_{\rm UAV}^2$  for the seven flights (ascent and descent) on a logarithmic scale. Most  $M_{\rm radar}^2 \gg M_{\rm UAV}^2$  occurrences (emphasized by the solid ellipse in Fig. 6) were found in the turbulent KH and CL regions. In addition, a bias due to radar instrumental (noise) thresholds can be seen for small values of  $M^2$  (dashed ellipse). These biases should not be taken into account in the interpretation of the results: the figure confirms that  $M_{\rm radar}^2 \approx M_{\rm UAV}^2$  but with a large dispersion, again partly due to altitude offsets between the thin  $M_{\rm radar}^2$ and  $M_{\text{IJAV}}^2$  peaks.

d. The steep negative humidity gradient (associated with a steep temperature inversion) at the interface between the ST and KH regions is a particular case worthy of separate study. This inversion was the signature of two humid and dry air masses of synoptic scale and persisted throughout the observation period in the UAV data. It produced large  $M_{\rm UAV}^2$ peaks. Figure 7 shows the time series of  $M_{\text{UAV}}^2$  and  $M_{\rm radar}^2$  selected at the altitude of the inversion (2.2– 2.6 km). The values compare very well. Their ratio is less than 2 for 7 cases out of 14 and less than 5 for 11 cases. However, there is a large discrepancy during UAV7 ( $\sim 11:00\,\mathrm{LT}$ ) since  $M_{\mathrm{radar}}^2$  profiles do not exhibit clear peaks. The selected values are somewhat arbitrary. Yet a thin echo layer was detected at the expected altitude ( $\sim 2.2 \, \mathrm{km}$ ) around flight UAV7 (see the inset in Fig. 5d) but tended to vanish for a while at the time of the flight. These time fluctuations contrast with the persistent nature of the gradient measured by the UAVs (it even strengthened further with time until  $\sim 13:00$  LT) indicating that turbulent diffusion was not effective within the inversion. However, turbulence was active below the inversion. Turbulent mixing at the edges of laminar gradient sheets is often suggested as an explanation for the fluctuating nature of the radar echoes generated by these gradients through a diffuse reflection mechanism (Röttger, 1980; Luce et al., 1995). We speculate that the roughness or corrugation of the gradient sheet surface can be the cause of the discrepancy during UAV7.

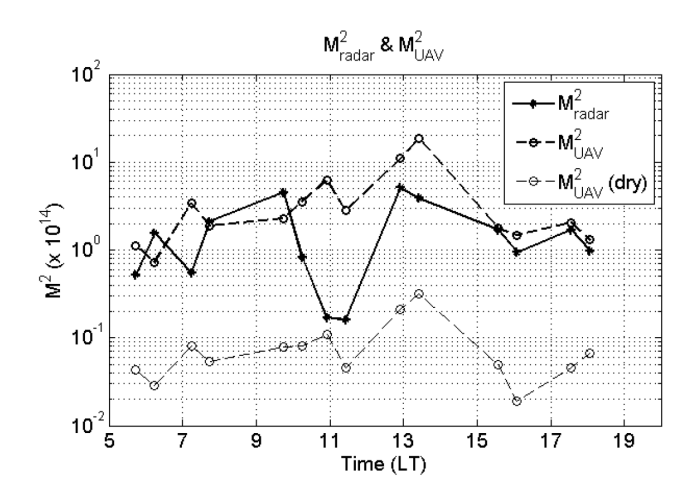


**Figure 7.** Time series of  $M_{\rm UAV}^2(\times 10^{14})$  (humid and dry) and  $M_{\rm radar}^2(\times 10^{14})$  for the selected inversion at the interface between the KH and ST regions.

- 2. A much more complex relationship exists between  $M_{\rm UAV}^2$  and  $M_{\rm radar}^2$  in the KH region. Highly variable features can be found in the range of the KH region and no clear properties can be concluded from the overall cases. However, it seems that some tendencies can be highlighted.
  - a. When coherent KH billows are probed by both instruments (e.g., Fig. 5a, UAV4 ascent) or when they were observed slightly prior to the UAV flight (e.g., Fig. 5a, UAV4 descent; Fig. 5d, UAV7 ascent), both  $M_{\rm UAV}^2$  and  $M_{\rm radar}^2$  profiles show strong peaks of similar amplitudes. However, the  $M_{\rm UAV}^2$  and  $M_{\rm radar}^2$ peaks are not observed at the same position giving the impression of large discrepancies. The  $M_{\rm radar}^2$ peaks during the ascent of UAV4 are the signature of the edges of the KH billows, where the gradients should be enhanced by the compression and stretching of the refractive index field (e.g., Woods, 1968). Therefore, the  $M_{\rm UAV}^2$  peaks should be interpreted in the same manner. The horizontal wavelength of the KH wave was 600 to 900 m so that the UAV and the radar did not probe the same billow structure at the same time and in the same portion of the billows. In addition, the different nature of the measurements makes it impossible to obtain agreement similar to that obtained in the ST region. Part of the disagreement can be explained by the horizontal variability. The thin solid line in Fig. 5a (UAV4 ascent) shows the 1 min averaged profile during the UAV flight. There are large discrepancies near the top of the KH region. The apparent trajectory of the UAV in the radar image suggests that the UAV crossed the top edge of a KH billow. But the measurements were made  $\sim 1 \, \mathrm{km}$  apart. Com-

parisons made with radar measurements collected 7 min before the UAV flight provide a better agreement, but they are not consistent with the hypothesis of frozen advection by the wind (analysis not shown).

Another substantial disagreement was observed during the ascent of UAV9 (Fig. 5f) for which the  $M_{\rm UAV}^2$  enhancements associated with the KH region were detected about 200 m above the corresponding  $M_{\rm radar}^2$  enhancements (solid black lines). The KH region was moving up and its vertical displacement was observed by the UAV first. Comparisons made with radar data collected about 10 min later provide a better qualitative agreement (dashed black lines).

b. An important feature can be noted when analyzing the KH region from flights UAV4 to UAV6. Schematically speaking, the detectable KH billows progressively disappeared; they were deep  $(\sim 300 \,\mathrm{m})$  and were clearly delineated during UAV4 (ascent). They were more diffuse and thinner during UAV5, and disappeared during UAV6 (see the insets of Fig. 5a, b and c). It is not necessarily a time evolution since the radar did not probe the same billows. But these observations can correspond to various stages of turbulence decay in the KH region. During UAV6 (ascent and descent) and UAV7 (ascent), there is a large discrepancy between  $M_{\rm UAV}^2$  and  $M_{\rm radar}^2$  contrasting with the results obtained in the ST region. Strong peaks of  $M_{\text{radar}}^2$  are observed at the core of the turbulent layer, while  $M_{\rm UAV}^2$  is at a minimum but enhanced at the edges of the layer. Therefore, the enhanced echo power associated with isotropic backscatter is not related to a strong background refractive index gradient. To our knowledge, this is the first time that this property is so clearly highlighted from radar and in situ  $M^2$  comparisons. It is likely due to the high resolution and the proximity of the measurements for ensuring that both the radar and the UAV observed the same atmospheric conditions. However, this observation should not be considered conclusive since many studies have reported turbulent layers with enhanced  $M^2$  but at much coarser resolutions (e.g., Hooper and Thomas, 1998).

It follows that the empirical K coefficient applied to radar echo power for estimating  $M^2$  and suitable for Fresnel scatter or reflection does not satisfy the conditions in the turbulent layer for which isotropic Bragg scatter is expected. It is consistent with the fact that radar equations differ according to the backscatter mechanisms (see Appendix A). But how can strong echoes be observed if the background refractive index gradient is weak? In such a case, the dominant parameter would be the outer

scale of turbulence  $L_0$  in the radar equation since  $P \sim L_0^{4/3} M^2$  (see Appendix A). Because the applied K coefficient contains unknown properties associated with Fresnel scatter or reflection model (A1.4b, A1.4c), it is not possible to make a qualitative estimate of  $L_0$  for fitting the observed radar echo power. But we speculate that  $L_0$  was enhanced during UAV6 and UAV7 (ascent). We note that  $M_{\rm UAV}^2$  and  $M_{\rm radar}^2$  agree well in the turbulent layer during UAV7 (descent). Radar echoes are now at a minimum, and this feature may indicate the late decay stage of turbulence (e.g., Fritts et al., 2011).

# 3. $M_{\text{UAV}}^2 \leq M_{\text{radar}}^2$ in convective clouds.

- a. As expected, significant peaks of  $M_{\rm UAV}^2$  and  $M_{\rm radar}^2$  were detected at the boundaries of convective clouds (dashed red lines in Fig. 5). Noting that the boundaries of cumulus clouds are highly irregular, as suggested by the bumpy shape of their signature in the radar echo power maps, the agreement is fairly good (Fig. 5). According to the mean wind speed observed at the cloud level (between 1.27 and 1.7 km), the cloud cells typically had a horizontal scale of  $\sim 1000\,\mathrm{m}$ . Therefore, the UAV and radar did not probe the same cells at the same time and more detailed conclusions cannot be obtained.
- b. Both  $M_{\rm UAV}^2$  and  $M_{\rm radar}^2$  in cloudy air can be weak and minimal (e.g., Fig. 5d, UAV7 (descent); Fig. 5f, UAV9; Fig. 5g, UV10). In contrast,  $M_{\rm radar}^2$  is much larger than  $M_{\rm UAV}^2$  during flight UAV4 (descent) (Fig. 5a) and to a lesser extent, during flight UAV6 (Fig. 5c). Several explanations are explored.
  - $M_{\rm UAV}^2$  given by Eq. (2) is not relevant for moist saturated conditions. A more proper expression for saturated air ( $M_{\rm sat}^2$ ) that takes into account the latent heat release resulting from vertical pseudoadiabatic displacements was proposed by Vaughan and Worthington (2000). It predicts a much lower value of  $M^2$  for saturated conditions. Therefore, comparisons with  $M_{\rm sat}^2$  would amplify the differences with  $M_{\rm radar}^2$  observed during UAV4 (descent) and thus would not explain the present observations.  $M_{\rm sat}^2$  is suitable for precipitating clouds or for moist air early after the rain ceased because the air refractive index irregularities are suppressed by precipitation (Vaughan and Worthington, 2000).
  - (Isotropic) turbulence in the convective cloud can be an alternative explanation (Fig. 3). If the turbulent nature of the cloud is a more important factor than air saturation, characteristics similar to those observed at the core of the KH turbulent layer and discussed in paragraph 2a

- may occur. Therefore, the difference would result from the irrelevant  $M^2$  model (and K factor).
- The generation of small-scale irregularities produced by the downward entrainment of non-saturated air from above at the cloud edges is the third possible explanation. Convective updrafts and downdrafts (±0.5 m s<sup>-1</sup> as observed by the MU Radar, not shown) would transport these irregularities vertically, explaining the belt-shaped morphology of the echoes near the cloud top (e.g., Fig. 3a).

#### 4 Summary and conclusions

The present paper describes new results of comparisons between the vertical profiles of the square of the generalized potential refractive index gradient  $M^2$  derived from the MU Radar and in situ measurements using small UAVs. The dataset was gathered during the ShUREX campaign (June 2015) at the Shigaraki MU observatory (Kantha et al., 2017). Comparisons were made in the lower atmosphere  $(1.27-\sim4.00\,\mathrm{km})$  for seven consecutive flights during the day from 05:44 to 17:33 LT on 7 June 2015. The study is significant because

- in situ measurements of pressure, temperature and humidity at 1 Hz and time responses similar to those provided by WMO radiosondes were made by IMET sonde sensors on the DataHawk UAV. This avoids the problem of horizontal wind drift (which can be a major issue for radiosondes hung below meteorological balloons when the wind is strong). The UAVs flew close to the MU Radar site at a constant horizontal distance of ∼1 km from the antenna array.
- comparisons could be made using UAV data collected during ascent and descent with a short time difference between the two and for seven consecutive flights over 13 h.
- 3. the colocation of the radar and UAV measurements made it possible to compare the  $M_{\rm UAV}^2$  profiles with nearly instantaneous  $M_{\rm radar}^2$  profiles (time averages of 1–4 min) reconstructed along the UAV flight paths. Almost all the previous studies based on radar and radiosonde data made comparisons using longer temporal averages (typically 30–60 min), without considering the height of the balloons during the averaging time.
- 4. the radar profiles were acquired in range imaging mode with Capon processing so that a much better vertical resolution (factor of  $\sim 10$  better) than the previous studies could be achieved. The  $M_{\rm UAV}^2$  profiles were calculated at a vertical resolution of 20 m and the radar pro-

- files were resampled at the UAV height so that quantitative comparisons at unprecedented time and range resolutions could be made. The present approach minimizes the low-pass filtering effects resulting from radar time integration and radar volume averaging.
- an attempt to compare absolute values was made based on an empirical calibration obtained from results of a previous study with the MU Radar operating in a similar mode.
- the agreements and discrepancies were interpreted in light of the prevailing backscatter mechanisms based on the radar echo aspect sensitivity and analyses of the dynamical conditions (e.g., Richardson number).

The main conclusions are as follows.

- 1. The high-resolution  $M_{\rm UAV}^2$  and  $M_{\rm radar}^2$  profiles agree well in stratified conditions, i.e., when the atmosphere is comprised of a stack of thin temperature and humidity gradient sheets between nearly homogeneous layers. The comparisons, made on linear scales, reveal similar levels of the  $M^2$  peaks and similar level dynamics with height.  $M_{\rm radar}^2$  peaks coincide with  $M_{\rm UAV}^2$  peaks, except on a few occasions. Some altitude differences can be explained by vertical air displacements due to small-scale internal waves. The study thus confirms that
  - a. the range imaging mode truly improves the range resolution without generating any ghost layer.
  - b. the UAV measurement configuration used (helical path) is suitable for measuring vertical gradients of temperature and humidity so that  $M_{\rm UAV}^2$  and  $M_{\rm radar}^2$  profiles are consistent with each other for stratified ambient conditions.
  - c. the vertical echo power is proportional to  $M^2$ , even on a scale down to a few tens of meters, when Fresnel scatter or reflection is expected to dominate. The calibration applied to the radar equation was suitable for reconstructing the  $M^2$  levels given by the UAV data. The MU Radar in range imaging mode thus provides a faithful image of the vertical distribution and time evolution of the humidity and temperature gradients as confirmed by measurements from UAV-borne in situ sensors down to a vertical scale of a few tens of meters.
  - d. the temperature and humidity gradients detected by the UAVs and the MU Radar extend horizontally over 1 km (the UAV–antenna-array distance) at least, and much more if we consider the advection by the wind. Both the radar and the UAV appear to have observed the same gradient layers.
- 2. The comparison is more qualitative in layers exhibiting Kelvin–Helmholtz billow activity, at least partly due to

the small horizontal scale (wavelength less than 1 km) and tilts of these coherent structures. The largest discrepancies between  $M_{\rm UAV}^2$  and  $M_{\rm radar}^2$  profiles could be observed when KH billows fade away, but the layer is still turbulent and echoes are isotropic. In some cases,  $M_{\rm UAV}^2$  was minimal while  $M_{\rm radar}^2$  was maximal at the core of the turbulent layer. This property was also observed in turbulent convective clouds. It is consistent with the fact that the Fresnel scatter model used (and the associated calibration factor K) should not be adapted to Bragg scatter. Therefore, absolute values of  $M_{\text{radar}}^2$ can differ from  $M_{\text{UAV}}^2$  in a turbulent layer. These differences, according to the prevailing backscattering mechanisms, emerged here very likely due to the high time and range resolution of the radar data. Accurate comparisons with in situ data were possible due to the nearly colocated and simultaneous measurements made by the UAV system.

3. Strong peaks of  $M_{\text{radar}}^2$  are observed at the core of a turbulent layer, while  $M_{\text{UAV}}^2$  is minimal but enhanced at the edges of the layer.

Data availability. Raw datasets are still under processing for other purposes and cannot be available to the public.

# Appendix A: Relationship between $M^2$ and VHF radar echo power at vertical incidence

Basically, there exist three main backscattering mechanisms for interpreting VHF radar clear-air echoes:

- 1. Bragg (3-D turbulent) scatter
- 2. Fresnel scatter from multiple and random gradients filling the radar resolution volume (the refractive index fluctuations are random along the vertical)
- 3. Fresnel or partial reflection (from a single, deterministic and localized gradient within the radar volume).

The mechanisms (1) and (2) reveal an  $M^2$  dependence of the echo power as shown by Gage and Balsley (1980). The third mechanism, deemed more unlikely for a long time and mainly due to the coarse range resolution of the VHF radars, also predicts an  $M^2$  dependence as indicated below.

1. (Isotropic) turbulent scatter (e.g., Tatarski, 1961; Van Zandt et al., 1978; Gage and Balsley, 1980; Hooper et al., 2004):

$$P = \frac{\alpha^2 P_{\rm t} A_{\rm e} \Delta z \alpha' L_0^{4/3} M^2}{\lambda^{1/3} z^2},\tag{A1}$$

where  $\alpha$  is a loss coefficient depending on the radar antenna and transmitting and receiving system performances,  $P_{\rm t}$ , the transmitted power,  $A_{\rm c}$ , the (effective) antenna array,  $\Delta z$ , the range resolution given by the transmitted pulse length  $\tau(\Delta z=1/2c\tau)$ , z, the altitude of the center of the range gate,  $\lambda$ , the radar wavelength,  $\alpha'$ , a ratio of eddy diffusion coefficients for the potential refractive index and heat,  $L_0$ , an outer scale of turbulence defined as the largest scale for which the turbulence is isotropic (Silverman, 1956; Tatarski, 1961),  $M^2$ , the squared *background* vertical gradient of generalized potential refractive index (Ottersten, 1969), on the scale of the radar range resolution  $\Delta z$ .

2. Fresnel scatter (e.g., Ottersten, 1969; Gage et al., 1985):

$$P = \frac{\alpha^2 P_t A_e^2 \Delta z F(\lambda)^2 M^2}{\lambda^2 z^2},$$
 (A2)

where  $F(\lambda)$  is a wavelength-dependent factor of proportionality, which relates the magnitude of the  $\lambda/2$  harmonic component of M over the altitude interval  $\Delta z$ . The other parameters are the same as in Eq. (A1).

3. Fresnel reflection (e.g., Röttger and Liu, 1978):

$$P = \frac{\alpha^2 P_{\rm t} A_{\rm e}^2}{4\lambda^2 z^2} |\rho|^2,$$

where  $|\rho|^2$  is the squared reflection coefficient produced by the refractive index gradient. In the Wentzel–Kramers–Brillouin approximation,

$$\rho = \frac{1}{2} \int_{-\Delta L/2}^{\Delta L/2} \frac{\mathrm{d}n}{\mathrm{d}z} \exp\left(-2kiz\right) \mathrm{d}z,$$

where  $\Delta L$  is the gradient depth. Introducing the normalizations,  $z^* = z/\Delta L$  and  $n^* = n/\Delta n$ ,

$$\rho = \frac{1}{2} \frac{\Delta n}{\Delta L} \Delta L \int_{-1/2}^{1/2} \frac{\mathrm{d}n^*}{\mathrm{d}z^*} \exp\left(-2ki \Delta L z^*\right) \mathrm{d}z^*,$$

i.e.,

$$|\rho|^2 = \frac{1}{4}M^2 \Delta L^2 \left| \int_{-1/2}^{1/2} \frac{\mathrm{d}n^*}{\mathrm{d}z^*} \exp\left(-2ki\,\Delta Lz^*\right) \mathrm{d}z^* \right|^2$$
$$= M^2 G(\lambda, \Delta L)^2.$$

Therefore, even for the Fresnel reflection model, the echo power is proportional to  $M^2$ :

$$P = \frac{\alpha^2 P_{\rm t} A_{\rm e}^2}{4\lambda^2 z^2} M^2 G(\lambda, \Delta L)^2.$$
 (A3)

But here,  $M^2$  is the squared value of a local gradient within the range gate.  $G(\lambda, \Delta L)^2$  is function of the depth *and shape* of the gradient.

All three models predict that echo power is proportional to  $M^2$ , but each model has an additional and a priori important factor:

$$L_0^{4/3}$$
 for the turbulent scatter, (A4a)

$$F(\lambda)^2$$
 for the Fresnel scatter, (A4b)

$$G(\lambda, \Delta L)^2$$
 for the Fresnel reflection. (A4c)

There is no reason to assume that these coefficients are constant with altitude. We can even expect extremely large variations in these (e.g., Woodman and Chu, 1989). The factors (A4a), (A4b) and (A4c) should dominate or at least could be a source of large discrepancies when comparing echo power and  $M^2$ . But this is not so, at least at first glance, from comparisons made in the literature.

To our knowledge, all previous comparisons with balloon data have been made at relative levels, mainly due to the difficulty of power calibration (e.g., Röttger, 1979; Green and Gage, 1980; Larsen and Röttger, 1983; Tsuda et al., 1988; Vincent et al., 1998; Hooper et al., 2004). Balloon-derived  $M^2$  has been compared with radar echo power at

zenith incidence without any assumption on the backscattering mechanism (which may be different at different altitudes, depending on turbulence and stability). All these studies concluded that, at least as a first approximation, the coefficients in Eqs. (A4a), (A4b) and (A4c) can be considered as constants.

The agreements were generally considered as "sufficiently good" for confirming that  $M^2$  is the dominant term, at least in a statistical sense and typically at range resolutions of 150– 1000 m and time averaging of 30-60 min. The first comparisons in range imaging mode by Chilson et al. (2001) and Luce et al. (2007) presented results of comparisons with the MU Radar at a vertical sampling of 50 m and a time averaging of 30 min for stratospheric heights. When there was disagreement at a given altitude, its interpretation was always hampered by the non-colocation of the radar and balloon measurements. In Luce et al. (2007), the authors showed that taking into account the wind advection can often improve the comparison agreements. Some discrepancies, as those shown by Vincent et al. (1998) in the  $M^2$  minima, are obviously due to the lack of radar echo power dynamics (radar noise contribution) and range smoothing effects. The radar is expected to detect the maxima better than the minima, and a linear representation of the comparisons as made by Hooper et al. (2004) and Luce et al. (2007) is also adopted here.

Competing interests. The authors declare that they have no conflict of interest

Acknowledgements. The authors thank JSPS for providing partial funding for the ShUREX 2015 campaign. We express our sincere thanks to M. Shiobara at the National Institute of Polar Research for providing the MPL system.

The topical editor, M. Salzmann, thanks two anonymous referees for help in evaluating this paper.

#### References

- Balsley, B. B., Svensson, G., and Tjernström, M.: On the scale-dependence of the gradient Richardson number in the residual layer, Bound.-Lay. Meteorol., 127, 57–72, 2008.
- Balsley, B. B., Lawrence, D. A., Woodman, R. F., and Fritts, D. C.: Fine-scale characteristics of temperature, wind, and turbulence in the lower atmosphere (0–1, 1300 m) over the south Peruvian coast, Bound.-Lay. Meteorol., 147, 165–178, doi:10.1007/s10546-012-9774-x, 2013.
- Bonin, T. A., Goines, D. C., Scott, A. K., Wainwright, C. E., Gibbs, J. A., and Chilson, P. B.: Measurements of temperature structure-function parameters with a small unmanned aerial system compared with a sodar, Bound.-Lay. Meteorol., 155, 417– 434, doi:10.1007/s10546-015-0009-9, 2015.
- Campbell, J. R., Hlavka, D. L., Welton, E. J., Flynn, C. J., Turner, D. D., Spinhirne, J. D., Scott, V. S., and Hwang, I. H.: Full-time, eye-safe cloud and aerosol lidar observation at atmospheric radiation measurement program sites: Instruments and data processing, J. Atmos. Ocean. Tech., 19, 431–442, 2002.
- Chilson, P. B., Palmer, R. D., Muschinski, A., Hooper, D. A., Schmidt, G., and Steinhagen, H.: SOMARE-99: A demonstrational field campaign for ultrahigh-resolution VHF atmospheric profiling using frequency diversity, Radio Sci., 36, 695–707, 2001.
- Dalaudier, F., Sidi F., Crochet, M., and Vernin, J.: Direct evidence of sheets in the atmospheric temperature field, J. Atmos. Sci., 51, 237–248, 1994.
- Fritts, D. C., Franke, P. M., Wan, K., Lund, T., and Werne, J.: Computation of clear-air backscatter from numerical simulations of turbulence: 2. Backscatter moments throughout the lifecycle of a Kelvin-Helmholtz instability, J. Geophys. Res., 116, D11105, doi:10.1029/2010JD014618, 2011.
- Fukao, S., Sato, T., Tsuda, T., Yamamoto, M., and Yamanaka, M. D.: MU radar – New capabilities and system calibrations, Radio Sci., 25, 477–485, 1990.
- Gage, K. S.: Radar observations of the free atmosphere: Structure and dynamics, in: Radar in Meteorology, chap. 28a, edited by: Atlas, D., 534–565, 1990.
- Gage, K. S. and Balsley, B. B.: On the scattering and reflection mechanisms contributing to clear air echoes from the troposphere, stratosphere and mesosphere, Radio Sci., 15, 243–257, 1980.
- Gage, K. S., Ecklund, W. L., and Balsley, B. B.: A modified Fresnel scattering for the parameterization of Fresnel returns, Radio Sci., 20, 1493–1501, 1985.

- Gossard, E. E.: Radar research on the atmospheric boundary layer, in: Radar in Meteorology, chap. 27a, edited by: Atlas, D., 477– 527, 1990.
- Green, J. L. and Gage, K. S.: Observations of stable layers in the troposphere and stratosphere using VHF radar, Radio Sci., 15, 395–405, 1980.
- Hocking, W. K. and Mu, P. K. L.: Upper and middle tropospheric kinetic energy dissipation rates from measurements of  $C_n^2$  review of theories in-situ investigations, and experimental studies using the Buckland Park atmospheric radar in Australia, J. Atmos. Sol.-Terr. Phy., 59, 1779–1803, 1997.
- Hooper, D. A. and Thomas, L.: Complementary criteria for identifying regions of intense atmospheric turbulence using lower VHF radar, J. Atmos. Sol.-Terr. Phy., 60, 49–61, 1998.
- Hooper, D. A., Arvelius, J., and Stebel, K.: Retrieval of atmospheric static stability from MST radar return signal power, Ann. Geophys., 22, 3781–3788, doi:10.5194/angeo-22-3781-2004, 2004.
- Kantha, L., Lawrence, D., Luce, H., Hashiguchi, H., Tsuda, T., Wilson, R., Mixa, T., and Yabuki, M.: Shigaraki UAV-Radar experiment (ShUREX 2015): Overview with some preliminary results, Progress in Earth and Planetary Science, submitted, 2017.
- Kirkwood, S., Belova, E., Satheesan, K., Narayana Rao, T., Rajendra Prasad, T., and Satheesh Kumar, S.: Fresnel scatter revisited comparison of 50 MHz radar and radiosondes in the Arctic, the Tropics and Antarctica, Ann. Geophys., 28, 1993–2005, doi:10.5194/angeo-28-1993-2010, 2010.
- Koishi, K. and Shiotani, M.: Water vapor and ozone variations in the tropical tropopause layer during the central equatorial pacific experiment campaign, J. Meteorol. Soc. Jpn., 90, 403–416, 2012.
- Kudo, A.: The generation of turbulence below midlevel cloud bases: The effect of cooling due to sublimation of snow, J. Appl. Meteorol. Clim., 52, 819–833, 2013.
- Kudo, A., Luce, H., Hashiguchi, H., and Wilson, R.: Convective instability underneath midlevel clouds: Comparisons between numerical simulations and VHF radar observations, J. Appl. Meteorol, Clim., 54, 2217–2227, 2015.
- Larsen, M. F. and Röttger, J.: Comparison of tropopause height and frontal boundary locations based on radar and radiosonde data, Geophys. Res. Lett., 10, 325–328, 1983.
- Larsen, M. F. and Röttger, J.: Observations of frontal zone and tropopause structures with a VHF Doppler radar and radiosondes, Radio Sci., 20, 1223–1232, 1985.
- Lawrence, D. A. and Balsley, B. B.: High-Resolution Atmospheric Sensing of Multiple Atmospheric Variables Using the DataHawk Small Airborne Measurement System, J. Atmos. Ocean. Tech., 30, 2352–2366, 2013.
- Lawrence, D. A., Frew, E., and Pisano, W.: Lyapunov vector fields for autonomous UAV flight control, AIAA J Guid. Control Dyn., 31, 1220–1229, 2008.
- Lawson, J., Vaughan, G., and Schultz, D. M.: Classifying fronts in data from a VHF wind-profiling radar, Atmos. Sci. Lett., 12, 375–380, 2011.
- Low, D. J., Reid, I. M., Vincent, R. A., and May, P. T.: Predicting VHF profiler performance from (p, T, q) soundings, in: Proc. of the Eighth Workshop on Technical and Scientific Aspects of MST Radar, edited by: Edwards, B., Sci. Comm. on Sol.-Terr. Phys. Secr., Boulder, Colorado, 294–297, 1998.

- Luce, H., Crochet, M., Dalaudier, F., and Sidi, C.: Interpretation of VHF ST radar vertical echoes from in-situ temperature sheet observations, Radio Sci., 30, 1002–1025, 1995.
- Luce, H., Yamamoto, M., Fukao, S., Hélal, D., and Crochet, M.: A Frequency radar Interferometric Imaging applied with High Resolution Methods, J. Atmos. Sol.-Terr. Phy., 63, 221–234, 2001.
- Luce, H., Hassenpflug, G., Yamamoto, M., and Fukao, S.: Comparisons of refractive index gradient and stability profiles measured by balloons and the MU radar at a high vertical resolution in the lower stratosphere, Ann. Geophys., 25, 47–57, doi:10.5194/angeo-25-47-2007, 2007.
- Luce, H., Takai, T., Nakamura, N., Yamamoto, M., and Fukao, S.: Simultaneous observations of thin humidity gradients in the lower troposphere with a Raman lidar and the VHF MU Radar, J. Atmos. Ocean. Tech., 27, 950–956, doi:10.1175/2010JTECHA1372.1, 2010.
- Luce, H., Hashiguchi, H., Kantha, L., Lawrence, D., Tsuda, T., Mixa, T., and Yabuki, M.: On the performance of the range imaging technique using UAVs during the ShUREX 2015 campaign, IEEE-TGRS, submitted, 2017.
- Nästrom, G. D. and Eaton, F. D.: Persistent layers of enhanced  $C_n^2$  in the lower stratosphere from VHF radar observations, Radio Sci., 36, 137–149, 2001.
- Ottersten, H.: Atmospheric structure and radar backscattering in clear air, Radio Sci., 4, 1179–1193, 1969.
- Röttger, J.: VHF radar observations of a frontal passage, J. Appl. Meteorol., 18, 85–91, 1979.
- Röttger, J.: Reflection and scattering of VHF radar signals from atmospheric reflectivity structures, Radio Sci., 15, 259–276, 1980.
- Röttger, J. and Larsen, M. F.: UHF/VHF radar techniques for atmospheric research and wind profiler applications, in: Radar in Meteorology, chap. 21, edited by: Atlas, D., 235–281, 1990.
- Röttger, J. and Liu, C. H.: Partial reflection and scattering of VHF radar signals from the clear atmosphere, Geophys. Res. Lett., 5, 357–360, 1978.
- Scipión, D. E., Lawrence, D. A., Milla, M. A., Woodman, R. F., Lume, D. A., and Balsley, B. B.: Simultaneous observations of structure function parameter of refractive index using a highresolution radar and the DataHawk small airborne measurement system, Ann. Geophys., 34, 767–780, doi:10.5194/angeo-34-767-2016, 2016.
- Silverman, R. A.: Turbulent mixing theory applied to radio scattering, J. Appl. Phys., 27, 699–705, 1956.

- Spinhirne, J. D.: Micro pulse lidar, IEEE T. Geosci. Remote Sens., 31, 48–55, 1993.
- Tatarski, I.: Wave propagation in a turbulent medium, translated by: Silverman, R. A., Graw-Hill, New York, 1961.
- Tsuda, T., May, P. T., Sato, T., Kato, S., and Fukao, S.: Simultaneous observations of reflection echoes and refractive index gradient in the troposphere and lower stratosphere, Radio Sci., 23, 655–665, 1988.
- van den Kroonenberg, A., Martin, T., Buschmann, M., Bange, J., and Vorsmann, P.: Measuring the wind vector using the autonomous mini aerial vehicle M2AV, J. Atmos. Ocean. Tech., 25, 1969–1982, 2008.
- Van Zandt, T. E., Green, J. L., Gage, K. S., and Clark, W. L.: Vertical profiles of refractivity turbulence structure constant: Comparison of observations by the Sunset radar with a new theoretical model, Radio Sci., 13, 819–829, 1978.
- Vaughan, G. and Worthington, R. M.: Effects of humidity and precipitation on VHF radar vertical beam echoes, Radio Sci., 6, 1389–1398, 2000.
- Vaughan, G., Howells, A., and Price, J. D.: Use of MST radars to probe the mesoscale structure of the tropopause, Tellus A, 47, 759–765, 1995.
- Vincent, R. A., Dullaway, S., MacKinnon, A., Reid, I. M., Zink, F., May, P. T., and Johnson, B. H.: A VHF boundary layer radar: First results, Radio Sci., 33, 845–860, 1998.
- Wilson, R., Luce, H., Hashiguchi, H., Nishi, N., and Yabuki, Y.: Energetics of persistent turbulent layers underneath mid-level clouds estimated from concurrent radar and radiosonde data, J. Atmos. Sol.-Terr. Phy., 118, 78–89, 2014.
- Woodman, R. F. and Chu, Y. H.: Aspect sensitivity measurements of VHF backscatter made with the Chung-Li radar: Plausible mechanisms, Radio Sci., 24, 113–125, 1989.
- Woodman, R. F., Michhue, G., Röttger, J., and Castillo, O.: The MPI-SOUSY-VHF radar at Jicamarca: High altitude resolution capabilities, extended Abstracts, 11th International Workshop on Technical and Scientific Aspects of MST Radar, Gadanki, India, Department of Science and Technology, Government of India, 4 pp., 2007.
- Woods, J. D.: Wave-induced shear instability in the summer thermocline, J. Fluid Mech., 32, 791–800, 1968.